

MAE 155B:
WIG Demonstrator Technical Report

Presented to the
University of California, San Diego
Department of Mechanical and Aerospace Engineering
MAE 155B
12 May 2025

Presented by:
Paul Manchala, Miles Puchner, Kyle Tomlinson, Arjun Trikannad

Contents

1	Introduction	7
2	Configuration Data	7
2.1	Geometry	7
2.2	Mass Properties	9
3	Aerodynamics	10
4	Propulsion	11
5	Flight Dynamics	12
5.1	Non-dimensional Stability Derivatives	12
5.2	Modal Analysis	12
6	Control System	13
6.1	Wing Leveler (Aileron Control)	13
6.2	Pitch Stabilization (Elevator Control)	15
6.3	Altitude Stabilization (Throttle Control)	16
6.4	Filters	16
6.5	Summary of Controllers	17
7	Conclusion	17
8	References	19
9	Appendix	20
9.1	Stability Derivative Equations	20

Figures

1	Three-view schematic with dimensions [cm] and an isometric view of the WIG vehicle.	8
2	Images of the completed WIG vehicle model.	8
3	(a) Lift coefficient and (b) drag coefficient versus angle of attack for the NACA 4415 airfoil at $Re = 1e6$; (c) the cross section (red) and mean camber line (yellow) are also shown [6]. . .	10
4	(a) Drag polar for in and out of ground effect and (b) aerodynamic efficiency versus the coefficient of lift for in and out of ground effect; analysis pulled from VSPaero simulations of the WIG model.	11
5	(a) Power required as a function of airspeed compared to the power available for varying rpm values for a 6x4.5 inch prop [8]; (b) Raw motor power available compared to available prop power at 10k rpm as a function of airspeed.	11
6	Aileron double feedback controller with roll command $\phi_{cmd}(s) = 0$ and saturation element limits $\pm a$	13
7	Wing leveler closed-loop poles for theoretical and experimental gain values; dynamics are based on VSPaero simulations.	14
8	Elevator double feedback controller with pitch command $\theta_{cmd}(s) \neq 0$ and saturation element limits $\pm a$; plant function coefficients A, B, C, and D are calculated from Eqn. 6.2.1.	15
9	Pitch stabilizer closed-loop zeros and poles for theoretical and experimental gain values; dynamics are based on VSPaero simulations.	16
10	Altitude single feedback controller with dead-band $\pm d$, contactor $\pm a$, and plant function $G(s)$	16

Tables

1	Geometric properties for the wing and horizontal tail.	8
2	OpenVSP component and total mass properties for the WIG vehicle; mass [g], CoG positions [cm], and moments of inertia [g-cm ²].	9
3	Measured total mass properties for the WIG vehicle; mass [g], CoG positions [cm], and moments of inertia [g-cm ²].	9
4	Non-dimensional stability derivatives (no ground effect) from VSPaero simulation; simulation parameters include $V = 10$ m/s, $\rho = 1.225$ kg/m ³ , and $\alpha = 2^\circ$. Derivatives relevant to Section 6 are in bold.	12
5	Control surface specific non-dimensional stability derivatives (no ground effect); simulation parameters include $V = 10$ m/s, $\rho = 1.225$ kg/m ³ , and $\alpha = 2^\circ$	12
6	Dimensional stability derivatives (no ground effect); simulation parameters include $V = 10$ m/s, $\rho = 1.225$ kg/m ³ , and $\alpha = 2^\circ$	13
7	Sign constraint on aileron controller gains due to physical considerations and control law $\delta_A(s) = [\phi_{cmd}(s) - \phi(s)]K_1 - K_2p(s)$; A_L and A_R are the left and right ailerons respectively.	14
8	Sign constraint on elevator controller gains due to physical considerations and control law $\delta_E(s) = [\theta_{cmd}(s) - \theta(s)]K_3 - K_4q(s)$	15
9	Controller summary for the WIG vehicle model.	17

List of Symbols

Aircraft Properties

\bar{c}	Mean geometric chord
\bar{q}	Dynamic pressure
δ_T	Total Throttle
δ_A	Aileron deflection
δ_E	Elevator deflection
ρ	Free-stream density
τ	Control surface effectiveness factor
τ_r	Roll mode time constant
b	Wingspan
I_{xx}	Moment of inertia about x-axis
I_{yy}	Moment of inertia about y-axis
I_{zz}	Moment of inertia about z-axis
m	Aircraft mass
S	Wing surface area
S_a	Aileron surface area
S_t	Horizontal tail surface area
T_p	Pilot Throttle
V	Free-stream airspeed
W	Aircraft weight
x_t	X-direction distance of horizontal tail from center of gravity
x_{cg}	Center of gravity location along x-direction
x_{np}	Aircraft neutral point
y_a	Y-direction distance from centerline to aileron
y_{cg}	Center of gravity location along y-direction
z_{cg}	Center of gravity location along z-direction

Aircraft Attitude

α	Angle of attack
β	Sideslip angle
ϕ	Roll
θ	Pitch
h	Altitude

p	Body fixed roll rate
q	Body fixed pitch rate
r	Body fixed yaw rate

Aerodynamic Coefficients

C_{D0}	Parasitic drag coefficient
C_D	Drag coefficient
C_{Fx}	X-direction force coefficient
C_{Fy}	Y-direction force coefficient
C_{Fz}	Z-direction force coefficient
C_L	Lift coefficient
C_{Ml}	Rolling moment coefficient
C_{Mm}	Pitching moment coefficient
C_{Mn}	Yawing moment coefficient
C_{Mx}	X-direction moment coefficient
C_{My}	Y-direction moment coefficient
C_{Mz}	Z-direction moment coefficient
C_S	Shear force coefficient

Non-dimensional Stability Derivatives

$C_{L\alpha_t}$	Lift curve slope of horizontal tail
$C_{L\alpha}$	Lift curve slope
$C_{l\delta A}$	Rolling moment coefficient derivative w.r.t. aileron deflection
$C_{L\delta E}$	Lift coefficient derivative w.r.t. elevator deflection
C_{lp}	Rolling moment coefficient derivative w.r.t. roll rate
C_{Lq}	Lift coefficient derivative w.r.t. pitch rate
$C_{m\alpha}$	Pitching moment coefficient derivative w.r.t. angle of attack
$C_{m\delta E}$	Pitching moment coefficient derivative w.r.t. elevator deflection
C_{mq}	Pitching moment coefficient derivative w.r.t. pitch rate

Dimensional Stability Derivatives

L_p	Rolling moment due to roll rate
$L_{\delta A}$	Rolling moment due to aileron deflection
M_α	Pitching moment due to angle of attack
$M_{\delta E}$	Pitching moment due to elevator deflection
M_q	Pitching moment due to pitch rate
Z_α	Z-direction force due to angle of attack
$Z_{\delta E}$	Z-direction force due to elevator deflection
Z_q	Z-direction force due to pitch rate

1 Introduction

A wing-in-ground (WIG) vehicle is an aircraft that utilizes the Wing-In-Ground effect, a phenomenon that occurs when "airflows interact with an external impervious surface [generating] a significant increase in static pressure below its surfaces, thereby creating an upward lifting force" [1]. In essence, it is an aircraft that flies incredibly close to a surface, like the water or ground, in order to experience increased lift and reduced drag. This reduced drag is caused by the ram-air effect, a ground effect caused by increased stagnation pressure below the wings, which "pushes the wing tip vortices laterally further away [...] significantly increasing their effective aspect ratio" [1].

These WIG vehicles have been explored and developed for a multitude of applications, including military, cargo, sea ambulances, and more. NASA has utilized winged aircraft meant to be shipped and flown on other celestial bodies, such as Mars. Most early designs, like the DSI Astroplane, resembled a high-performance sailplane that was powered by a hydrazine piston engine. However, one of the most difficult challenges in the development of these vehicles is the restrictions in size and weight for stowing and launching to Mars. The DSI Astroplane required six wing folds, three fuselage folds, and a folding propeller to fit inside a Viking-like aeroshell. The Mars Airplane Package (MAP), a concept developed as a challenge to fly on Mars, had limited storage for an aeroshell with only a 0.8 meter diameter. The Aerial Regional-Scale Environmental Survey of Mars (ARES) mission was limited to a Viking-derivative aeroshell shape with an internal diameter of 2.48 meters [2].

In addition, the crash of the Ingenuity helicopter on Mars raises questions about the best design for an aerial vehicle on other planets. The cause of the crash was determined to be the failure of the onboard navigation sensors to discern the features of Mars' relatively smooth ground surface. Based on a WIG vehicle's apt ability to fly close to smooth surfaces, like sandy terrain or ice, it can be a prime candidate to replace rotorcraft as the aircraft of choice.

The goal of the WIG demonstrator project is to develop a proof of concept that can exhibit the aerial mobility of the WIG vehicle for use on other celestial bodies, while limited in wingspan and weight. The WIG demonstrator is a complex engineering problem due to its additional requirements in design. The fuselage must be both aerodynamic and hydrodynamic, as Titan boasts liquid methane seas greater than 1000 feet deep [3]. As a result, the aircraft's structure must also be "designed for increased strength and stiffness to carry the hydrodynamic loads at the expense of structural weight" [1]. The material of the fuselage must also be taken into consideration due to the possibility of controlled flight into terrain. The material and design need to allow the aircraft to slide and skim across the surface, rather than catching and flipping. In addition, the wings should have a low aspect ratio and be relatively short in wingspan. The ram-air effect increases the wing's aspect ratio and gives the benefit of a lower induced drag for a wing with a lower aspect ratio, saving structural weight. The horizontal stabilizer must also have a significant surface area to compensate for the "change in pitching moment if the vehicle reaches an altitude that comes out of ground-effect" [1]. Therefore, the vehicle must fit a multitude of engineering and mission requirements, ultimately being able to fly both in and out of the ground effect, and sustain consistent collision with smooth terrain and liquids.

The benefits of a WIG vehicle cannot be understated. The use of the wing-in-ground effect can allow for flight and exploration on other planets, as well as be used for applications on Earth. With the use of the ram-air effect and ground effect, smaller wings can be used for the same payload, allowing for the creation of very large aircraft without the increased structural weight. Our WIG demonstrator capstone will allow us to test and develop WIG aircraft in an effort to determine the viability of its use on celestial bodies like Mars and Titan.

2 Configuration Data

2.1 Geometry

Accurate geometrical modeling of the WIG vehicle from OpenVSP is shown in Fig. 1. Specific geometric properties for the wing and horizontal tail are listed in Tab. 1. The main wing's medium to low aspect ratio was chosen to maximize the extra lift obtained from the ground effect, while maintaining versatility for free flight. The likely classification for this vehicle would be a type B WIG, with primary operation in

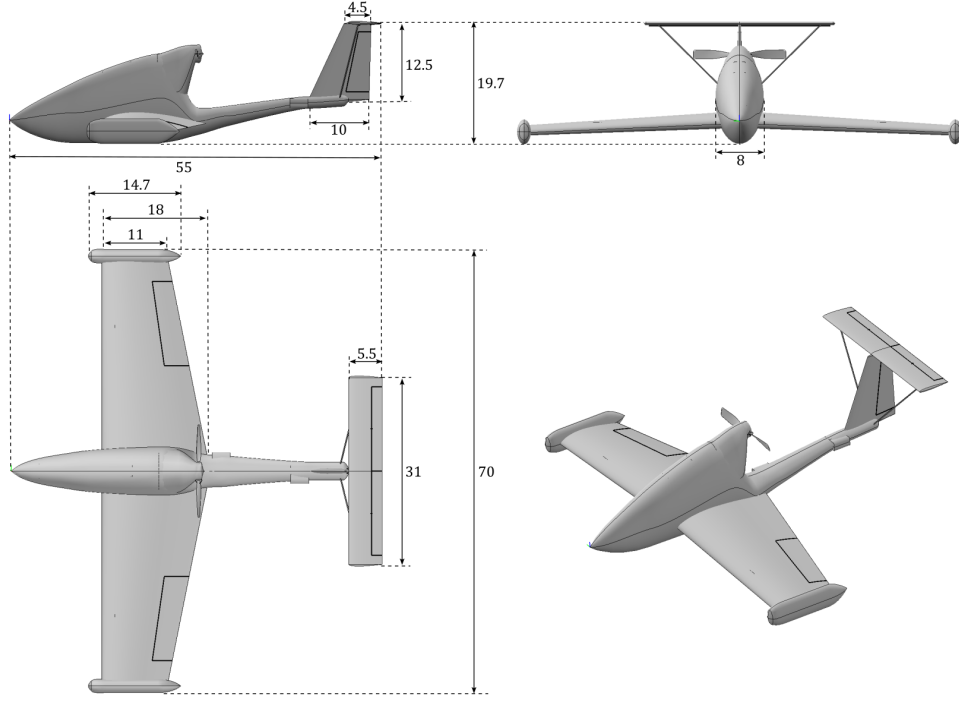


Fig. 1: Three-view schematic with dimensions [cm] and an isometric view of the WIG vehicle.

ground effect while retaining the ability to deviate to higher altitudes for obstacle avoidance or emergency situations [4].

Table 1: Geometric properties for the wing and horizontal tail.

	Span [cm]	Area [cm ²]	Mean Chord [cm]	Root Chord [cm]	Tip Chord [cm]	Aspect Ratio
Wing	70	1015	14.5	18	11	4.83
Tail	31	170.5	5.5	5.5	5.5	5.64

Images of the WIG model as-built are shown in Fig. 2. The fuselage, wings, tail, skids, and control surfaces are constructed out of foam; hollow carbon fiber rods are used as braces for the tail. Four servomotors control the two ailerons, rudder, and elevator. Automatic controllers, as described in Section 6, are used to control the ailerons, elevator, and throttle; the rudder is controlled by pilot input alone, while the throttle controller is additive to the pilot input. There is no pilot control of the ailerons or elevator.



Fig. 2: Images of the completed WIG vehicle model.

2.2 Mass Properties

Mass properties of each component, and the vehicle as a whole, were derived from OpenVSP. To do so, accurate modeling of component sizes, densities, and positions was required; the results are listed in Tab. 2.

Table 2: OpenVSP component and total mass properties for the WIG vehicle; mass [g], CoG positions [cm], and moments of inertia [g-cm²].

	Mass	x_{cg}	y_{cg}	z_{cg}	I_{xx}	I_{yy}	I_{zz}
Fuselage	72.34	21.15	0	2.554	955.7	7562	7057
Motor Housing	4.269	28.66	0	8.93	23.19	19.78	16.76
Wing	68.13	21.29	0	-0.616	21570	950.1	22440
Skid (Right)	3.658	19.93	35.73	-1.866	5.078	60.66	57.96
Skid (Left)	3.658	19.92	-35.73	-1.866	5.09	60.68	57.98
Vert. Tail	1.96	55.13	0	8.498	21.09	29.48	8.585
Horz. Tail	2.91	58.27	0	16.06	238.8	5.195	243.8
Motor	20.91	30.12	0	11.02	12.25	8.812	10.68
Battery	40.58	6.303	0	0.4429	96.31	101.1	44.91
Receiver	6.784	7.884	0	1.75	12.9	12.99	5.119
ESC	18.12	17.83	0	8.39	13.05	43.87	43.96
Aileron Servo (Right)	11.1	18.75	22.83	-0.9836	10.74	11.33	17.88
Aileron Servo (Left)	11.1	18.75	-22.83	-0.9836	10.74	11.33	17.87
Elevator Servo	11.09	47.65	-0.5738	2.787	10.78	11.29	17.9
Rudder Servo	11.09	34.74	1.557	0.4918	10.81	11.3	17.94
Additional Electronics / Wires	50	11.3	0	2.283	0	0	0
Added Weight	56.3	2.826	0	0	0	0	0
Total	394	17.37	0.02633	1.959	48390	59990	97620

The total mass properties for the as-built model are in Tab. 3. The moments of inertia were determined from the manual timing of swing balance and bifilar torsion pendulum periods [5]. The equations for the experimental determination of the moments of inertia are

$$I_{nn} = mL\left[\frac{T_n^2 g}{4\pi^2} - L\right] \quad \text{for } n = x, y \quad \text{and} \quad I_{zz} = \frac{mgT_z^2 d^2}{16\pi^2 D} \quad (2.2.1)$$

with T_i as the period for the respective pendulum type i , L as the pendulum length, d as the bifilar pendulum distance between verticals, and D as the bifilar pendulum filament length. The experimental periods T_x , T_y , and T_z were determined to be 1.962, 1.966, and 1.978 seconds, respectively, with $L = 0.940$ m, $D = 0.432$ m, and $d = 0.229$ m.

Table 3: Measured total mass properties for the WIG vehicle; mass [g], CoG positions [cm], and moments of inertia [g-cm²].

	Mass	x_{cg}	I_{xx}	I_{yy}	I_{zz}
Total	396.6	18	62428	76980	116660

The discrepancies between the modeled and experimentally measured moments of inertia are due in part to the modeling of certain masses as point masses within OpenVSP and human error when determining the pendulum periods. The latter is likely the most significant error, as small changes in the periods (hundredths of a second) result in large changes in the calculated moments of inertia. That said, the general trend and order of magnitude are similar between the two methods.

3 Aerodynamics

Once deployed on the surface of a celestial body, the model is a likely candidate for reconnaissance and scientific missions, where high-resolution imaging and atmospheric sampling would take place over long ranges. As a result, a NACA 4415 airfoil cross section was chosen for the main wing to meet these specific mission requirements. The lift and drag curves, and cross section for the airfoil are shown in Fig. 3.

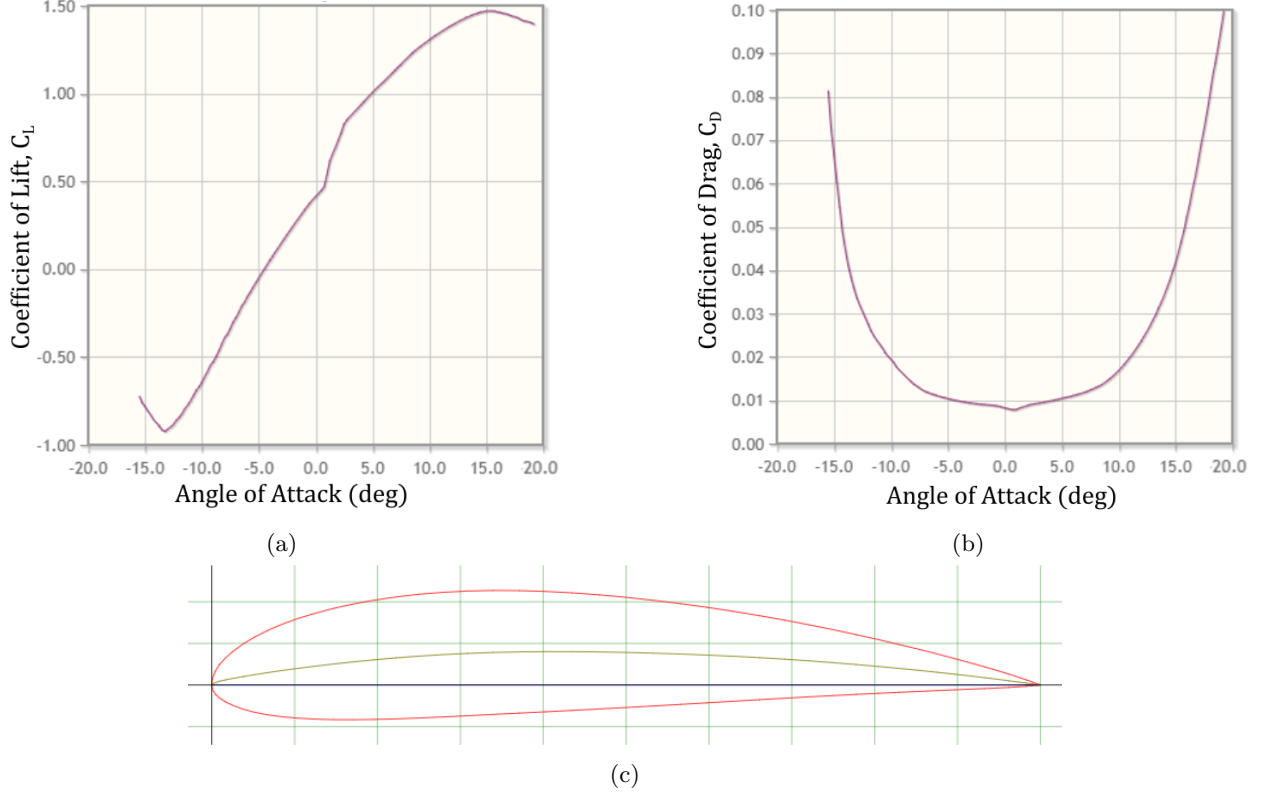


Fig. 3: (a) Lift coefficient and (b) drag coefficient versus angle of attack for the NACA 4415 airfoil at $Re = 1e6$; (c) the cross section (red) and mean camber line (yellow) are also shown [6].

Understanding that $V_{stall} = \sqrt{\frac{2W}{\rho S C_{L,max}}}$, the already large maximum coefficient of lift (roughly 1.5) stands to increase even more under the ground effect, subsequently lowering the stall speed of the aircraft significantly. Combined with Titan's significantly denser atmosphere, the NACA 4415 could achieve extremely low flight speeds before stall, allowing for better imaging capabilities and detailed data collection. Seeing as $D = \frac{1}{2}\rho V^2 S C_D$, low flight speeds would also significantly decrease the total drag acting on the aircraft, resulting in better flight efficiency and longer mission duration before needing to refuel/recharge. Finally, the cambered nature of the airfoil promises significant lift generation at low angles of attack without the need for control surface deflection, allowing for more stable control.

The benefits of the ground effect are more clearly seen in Fig. 4. A plot of the drag polar for both cases reveals a 17.3% reduction in the induced drag factor (K) when the WIG vehicle flies at a 25 cm altitude ($\frac{h}{b} = 35.7\%$). Additionally, for a given C_L , the aerodynamic efficiency for the model is greater under the ground effect than when in free flight. In fact, Fig. 4b shows that the ground effect yields at least a 10% increase in aerodynamic efficiency at all coefficients of lift greater than 0.3. Such an effect ultimately lowers energy consumption for the aircraft while increasing its maximum range and endurance.

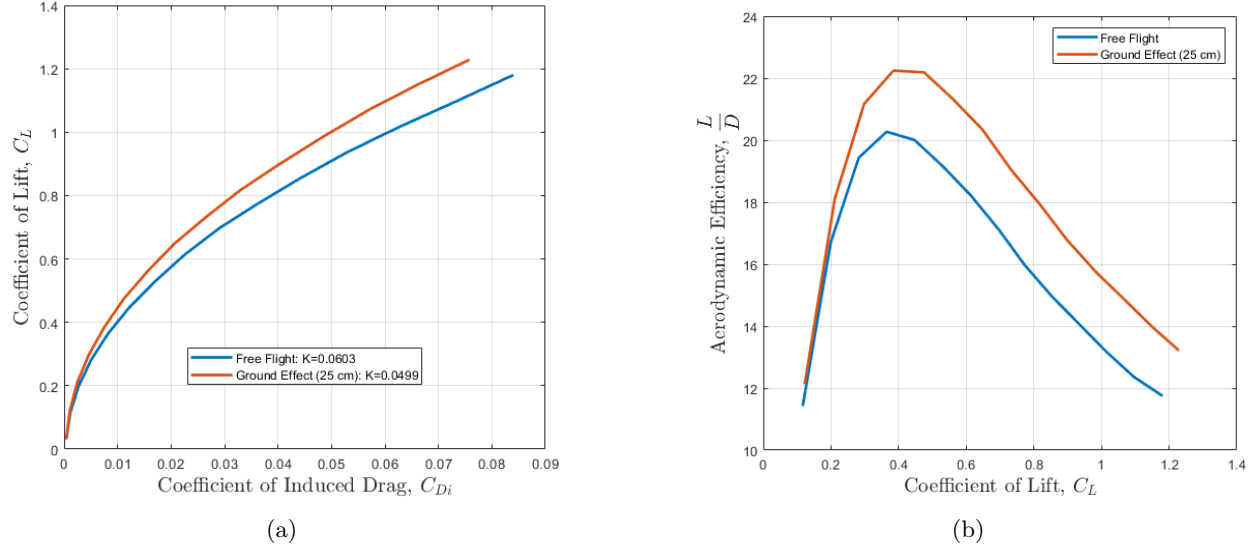


Fig. 4: (a) Drag polar for in and out of ground effect and (b) aerodynamic efficiency versus the coefficient of lift for in and out of ground effect; analysis pulled from VSPaero simulations of the WIG model.

4 Propulsion

Application of the induced drag factors from Fig. 4 with a parasitic drag (C_{D0}) from VSPaero of 0.041 yields the power required versus power available plots shown in Fig. 5a. Determination of the power required curves follows from

$$P_R = \frac{1}{2}\rho V^3 S C_{D0} + \frac{2KW^2}{\rho V S} \quad (4.0.1)$$

where W is the weight of the aircraft, and the remaining variables follow from previous definitions [7].

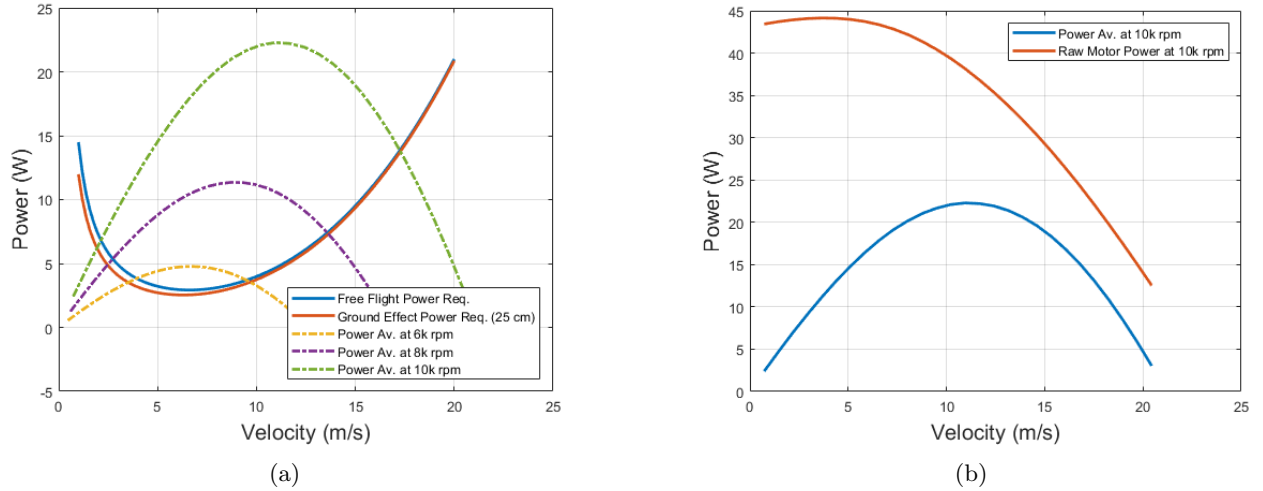


Fig. 5: (a) Power required as a function of airspeed compared to the power available for varying rpm values for a 6x4.5 inch prop [8]; (b) Raw motor power available compared to available prop power at 10k rpm as a function of airspeed.

At the highest prop rotation speed (10k rpm), the max speed for sustainable flight is seen to be roughly 17.5 m/s. This is ultimately much faster than needed, with nominal flight speeds being around 10 m/s. As

a result, the upper limit of the 6k rpm line is nearly sufficient for reaching this speed, and even offers a trim condition just shy of 10 m/s. It is worth noting that the power required is slightly less under the ground effect for airspeeds less than 10 m/s, although this trend diminishes for higher airspeeds.

In the event that greater airspeeds need to be reached, Fig. 5b also displays the raw motor power needed to reach a 10k rpm prop speed. Maxing out at nearly 45 W, battery sizing must be large enough to supply this power consumption while also powering other electronics onboard. Use of a 7.4 V, 800 mAh battery with a 45 C discharge yields a max continuous power of 266.4 W. At nearly 6 times the power consumption of the motor at 10k rpm, this battery size will be more than capable of supplying power to the motor and remaining onboard electronics.

5 Flight Dynamics

5.1 Non-dimensional Stability Derivatives

To determine the flight dynamics of the aircraft, accurate modeling of the weight, shape, and size were constructed in OpenVSP. Aerodynamic simulations through VSPaero allowed for theoretical stability derivatives to be calculated. Simulation parameters include a nominal 10 m/s airspeed at sea-level, and an angle of attack of 2° . The resulting non-dimensional stability derivatives are below in Tab. 4; the static margin for these values is 24.8% with a neutral point (x_{np}) of 22.2 cm from the nose.

Table 4: Non-dimensional stability derivatives (no ground effect) from VSPaero simulation; simulation parameters include $V = 10$ m/s, $\rho = 1.225$ kg/m³, and $\alpha = 2^\circ$. Derivatives relevant to Section 6 are in bold.

Coefficient	With respect to...				
	α	β	p	q	r
C_{Fx}	-0.4073892	-0.0058540	-0.0182226	-0.2471732	-0.0068184
C_{Fy}	0.0001455	-0.3040869	0.0702308	-0.0004399	0.2894400
C_{Fz}	4.6731814	-0.0689021	0.0099177	8.3551802	0.0022847
C_{Mx}	0.0000658	0.0204501	0.4435395	-0.0017444	-0.1280127
C_{My}	-1.1561152	0.0211177	0.0021985	-10.8823828	0.0012737
C_{Mz}	0.0000590	-0.1516869	0.0356843	-0.0000329	0.1568211
C_L	$C_{L\alpha} = \mathbf{4.6603283}$	-0.0686559	0.0105477	$C_{Lq} = \mathbf{8.3587166}$	0.0025213
C_D	0.3126680	-0.0031512	-0.0178654	0.0445690	-0.0067345
C_S	0.0001455	-0.2805613	0.0702308	-0.0004399	0.2894400
C_{Ml}	-0.0000658	-0.0204501	$C_{lp} = \mathbf{-0.4435395}$	0.0017444	0.1280127
C_{Mm}	$C_{m\alpha} = \mathbf{-1.1561152}$	0.0211177	0.0021985	$C_{mq} = \mathbf{-10.8823828}$	0.0012737
C_{Mn}	-0.0000590	0.1516869	-0.0356843	0.0000329	-0.1568211

Non-dimensional stability derivatives specific to the control surfaces will also be of use. Equations specific to these derivatives can be found in the Appendix (Section 9.1); however, their values are summarized below in Tab. 5.

Table 5: Control surface specific non-dimensional stability derivatives (no ground effect); simulation parameters include $V = 10$ m/s, $\rho = 1.225$ kg/m³, and $\alpha = 2^\circ$

$C_{l\delta A}$	$C_{L\alpha t}$	$C_{L\delta E}$	$C_{m\delta E}$
0.1102	4.1866552	0.3516	-0.7518

5.2 Modal Analysis

Calculation of the roll and short-period modes, and their characteristics, follows from the determination of specific dimensional derivatives. Equations for these derivatives are listed in the Appendix (Section 9.1);

Table 6: Dimensional stability derivatives (no ground effect); simulation parameters include $V = 10$ m/s, $\rho = 1.225$ kg/m³, and $\alpha = 2^\circ$.

$L_{\delta A}$ [1/s ²]	L_p [1/s]	$M_{\delta E}$ [1/s ²]	M_α [1/s ²]	M_q [1/s]	$Z_{\delta E}$ [m/s ²]	Z_α [m/s ²]	Z_q [m/s]
99.101	-13.961	-112.97	-173.73	-11.856	-5.5484	-74.178	-0.9562

however, their values are summarized in Tab. 6. The roll mode and roll mode time constant of the aircraft follow as

$$\frac{p(s)}{\delta_A(s)} = \frac{L_{\delta A}}{s - L_p} = \frac{99.101}{s + 13.961} \quad \text{and} \quad \tau_r = \frac{-1}{L_p} = \frac{-1}{-13.961} = 0.0716 \text{ sec.} \quad (5.2.1)$$

The short-period mode follows as

$$\frac{q(s)}{\delta_E(s)} = \frac{(M_{\delta E})s + \frac{1}{V}(M_\alpha Z_{\delta E} - Z_\alpha M_{\delta E})}{s^2 - (\frac{Z_\alpha V}{V} + M_q)s + (\frac{Z_\alpha}{V} M_q - M_\alpha - \frac{Z_q}{V})} = \frac{As + B}{s^2 + Cs + D} = \frac{-112.97s - 741.57}{s^2 + 19.273s + 261.76} \quad (5.2.2)$$

with characteristic roots at $-9.6367 \pm 12.9960i$. These roots yield a natural frequency and damping of 16.1791 rad/s and 0.5956, respectively.

Although the short-period mode's natural frequency is much larger compared to full-scale conventional aircraft [9], it is not unreasonable due to the scale of the WIG demonstrator. The small and lightweight nature of the model makes it much stiffer relative to its total mass, ultimately inciting quick responses to perturbations. That said, the damping is within the expected range, allowing for decreased oscillations and overshoot in the pitch response. The roll mode time constant is also within the expected range, yielding fast and crisp response that avoids input lag errors and subsequent overcorrection. However, such a fast response means that controller gains must be well-tuned to ensure that excessive overshoot does not cause instability.

6 Control System

6.1 Wing Leveler (Aileron Control)

The primary advantage of a WIG vehicle over traditional aircraft is the utilization of the "wing-in-ground" effect, which requires a sufficiently low altitude. However, with this advantage comes limited mobility in the roll of the aircraft. Moderate changes in the roll angle at such low altitudes would result in wing contact with the ground, and subsequently, vehicle loss at high speeds. Such a constraint on the aircraft's maneuvering motivates the need for an automatic wing leveler to ensure that WIG vehicles remain a viable option for reconnaissance missions on the surface of Titan.

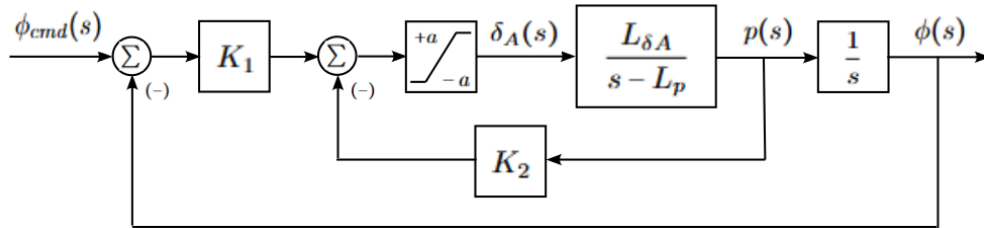


Fig. 6: Aileron double feedback controller with roll command $\phi_{cmd}(s) = 0$ and saturation element limits $\pm a$.

To achieve this, the control system presented in Fig. 6 was integrated onto the onboard computer. Use of an IMU allows for continuous pulls of the aircraft's current roll angle (ϕ) and body-fixed roll rate (p) for use in the feedback loop. The saturation element ensures that the physical limit of the ailerons is not exceeded ($a = \pm 25^\circ$), and the double feedback loop allows more control over the response time and damping of the system. It should be noted that the two ailerons use the same control system above, but deflect equally in opposite directions to induce a counter rolling moment.

The closed-loop transfer function for the wing leveler follows from Fig. 6 as

$$\frac{\phi(s)}{\phi_{cmd}(s)} = \frac{L_{\delta A} N K_1}{s^2 + (L_{\delta A} N K_2 - L_p)s + L_{\delta A} N K_1}, \quad (6.1.1)$$

where dimensional derivatives $L_{\delta A}$ and L_p follow from Section 5.2, and N is an equivalent gain to model the saturation element [10]. To simplify the analysis in determining the gains, it is assumed that deviation from level flight will begin slowly, with the aileron deflection angle required to correct the deviation being much smaller than its physical limit. Such an assumption allows N to be set to unity.

Further analysis of Fig. 6 reveals that aileron deflection is related to roll and roll rate by the control law $\delta_A(s) = [\phi_{cmd}(s) - \phi(s)]K_1 - K_2 p(s)$. By defining positive deflection as the left aileron down and the right aileron up to impose a positive rolling moment in the body-fixed frame, the gains K_1 and K_2 are both restricted to be positive, as shown in Tab. 7.

Table 7: Sign constraint on aileron controller gains due to physical considerations and control law $\delta_A(s) = [\phi_{cmd}(s) - \phi(s)]K_1 - K_2 p(s)$; A_L and A_R are the left and right ailerons respectively.

Scenario	Goal	Aileron Action	Defl. Sign	Req. Gain Sign
$\phi_{cmd}(s) > \phi(s)$	Induce pos. roll	A_L down; A_R up	$\delta_A(s) > 0$	$K_1 > 0$
$\phi_{cmd}(s) < \phi(s)$	Induce neg. roll	A_L up; A_R down	$\delta_A(s) < 0$	$K_1 > 0$
$p(s) \gg 0$	Induce neg. roll	A_L up; A_R down	$\delta_A(s) < 0$	$K_2 > 0$
$p(s) \ll 0$	Induce pos. roll	A_L down; A_R up	$\delta_A(s) > 0$	$K_2 > 0$

Verification of these signs follows from imposing the Routh-Hurwitz stability criterion [11] on the denominator of Eqn. 6.1.1. Knowing that $L_{\delta A} > 0$ and $L_p < 0$ (Eqn. 5.2.1), further constraints on the gains are found to be $K_1 > 0$ and $K_2 > \frac{L_p}{L_{\delta A}} < 0$. Therefore, to satisfy these constraints and those from Tab. 7, K_1 and K_2 must be positive for the system to perform as expected and be stable.

After manipulation of the characteristic equation into root locus form with variable gain K_2 , theoretical testing yielded final K_1 and K_2 values of 1.5 and 0.05, respectively. Of course, the aforementioned values are theoretical approximations based on stability simulations from OpenVSP. After experimental response testing, actual values for K_1 and K_2 were found to be 0.8 and 0.02, respectively. The lower roll rate gain ensures that twitches to small, quick perturbations were not as emphasized in the aileron movement. The closed-loop poles for the theoretical and experimental gain values are displayed in Fig. 7.

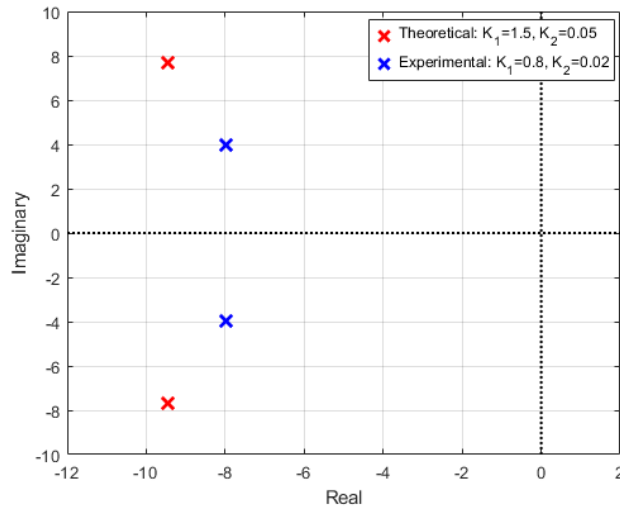


Fig. 7: Wing leveler closed-loop poles for theoretical and experimental gain values; dynamics are based on VSPaero simulations.

6.2 Pitch Stabilization (Elevator Control)

Following earlier logic, maintaining a steady pitch ensures that contact of the nose or tail of the aircraft with the ground is avoided at low altitudes. Modification of Fig. 6 with pitch-related quantities yields the control system presented in Fig. 8.

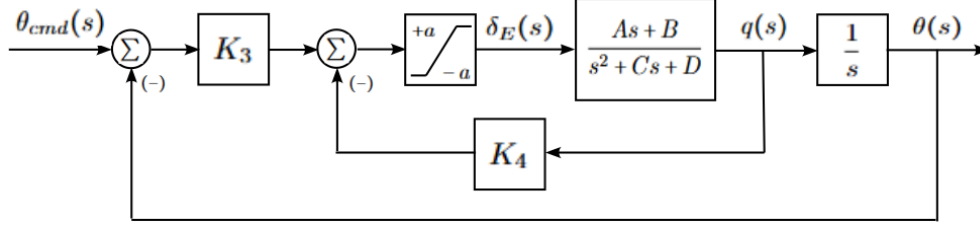


Fig. 8: Elevator double feedback controller with pitch command $\theta_{cmd}(s) \neq 0$ and saturation element limits $\pm a$; plant function coefficients A , B , C , and D are calculated from Eqn. 6.2.1.

Similar to Section 6.1, IMU data pulls continuous pitch and rate data for use in the system. A saturation element prevents the deflection from exceeding the elevator's physical limits ($a = \pm 20^\circ$), and the double feedback loop offers more control over shaping the system to desired specifications. The closed-loop transfer function associated with Fig. 8 follows as

$$\frac{\theta(s)}{\theta_{cmd}(s)} = \frac{(As+B)NK_3}{s^3 + (C + ANK_4)s^2 + (D + ANK_3 + BNK_4)s + BNK_3}, \quad \begin{bmatrix} A \\ B \\ C \\ D \end{bmatrix} = \begin{bmatrix} M_{\delta E} \\ \frac{1}{V}(M_\alpha Z_{\delta E} - Z_\alpha M_{\delta E}) \\ -(\frac{Z_\alpha}{V} + M_q) \\ \frac{1}{V}(Z_\alpha M_q - Z_q) - M_\alpha \end{bmatrix} \quad (6.2.1)$$

where coefficients A , B , C , and D follow from Section 5.2, and N is an equivalent gain to model the saturation element. Assuming deviations in pitch occur slowly such that saturation of the elevator is not reached, N can be set to unity.

Governed by the control law $\delta_E(s) = [\theta_{cmd}(s) - \theta(s)]K_3 - K_4q(s)$, elevator deflection is best defined as positive when the aircraft moves nose-down (elevator trailing edge down) to impose a negative pitching moment in the body-fixed frame. In doing so, physical considerations restrict the gains K_3 and K_4 to be negative, as shown in Tab. 8.

Table 8: Sign constraint on elevator controller gains due to physical considerations and control law

$$\delta_E(s) = [\theta_{cmd}(s) - \theta(s)]K_3 - K_4q(s).$$

Scenario	Goal	Elevator Action	Defl. Sign	Req. Gain Sign
$\theta_{cmd}(s) > \theta(s)$	Induce pos. pitch	Up	$\delta_E(s) < 0$	$K_3 < 0$
$\theta_{cmd}(s) < \theta(s)$	Induce neg. pitch	Down	$\delta_E(s) > 0$	$K_3 < 0$
$q(s) \gg 0$	Induce neg. pitch	Down	$\delta_E(s) > 0$	$K_4 < 0$
$q(s) \ll 0$	Induce pos. pitch	Up	$\delta_E(s) < 0$	$K_4 < 0$

For the current WIG configuration, $A < 0$, $B < 0$, $C > 0$, and $D > 0$ (Eqn. 5.2.2). Knowing the sign of each coefficient allows the Routh-Hurwitz criterion of stability to be employed. Ensuring each coefficient of the denominator of Eqn. 6.2.1 is positive produces $K_4 < \frac{-C}{A} > 0$, $K_3 < 0$, and $K_4 < \frac{-(D+AK_3)}{B} > 0$ as additional constraints. Comparing these conditions with those from Tab. 8 shows that K_3 and K_4 must be negative for the system to perform as expected and be stable.

Analysis of the root locus plot of the characteristic equation with variable gain K_4 yielded theoretical K_3 and K_4 values of -0.4 and -0.05 respectively. Once again, these values assumed simplifications in their derivation and were computed from stability simulation results. As such, further experimental response testing proved -0.3 and -0.01 to be more fitting values for K_3 and K_4 , respectively. A similarly decreased pitch rate gain allowed for less sporadic elevator movement due to motor vibrations at high throttle values. The closed-loop poles and zeros for the theoretical and experimental gain values are shown in Fig. 9.

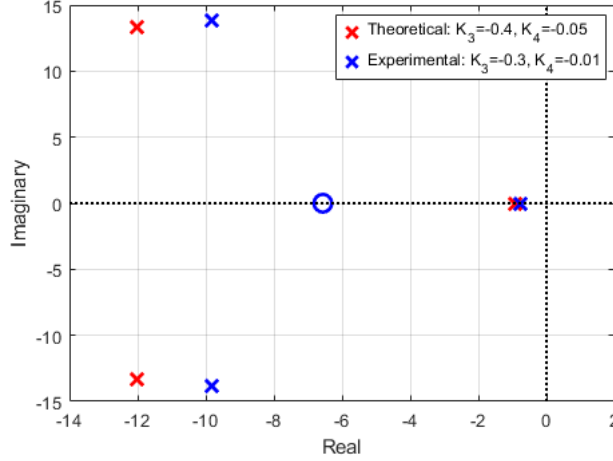


Fig. 9: Pitch stabilizer closed-loop zeros and poles for theoretical and experimental gain values; dynamics are based on VSPaero simulations.

6.3 Altitude Stabilization (Throttle Control)

Theoretical analysis of a throttle controller proves significantly more difficult due to the complex dynamics of the motor. Fig. 10 displays the altitude control system implemented on the WIG vehicle.

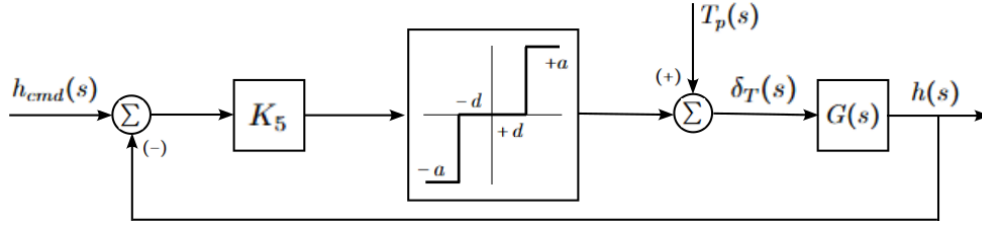


Fig. 10: Altitude single feedback controller with dead-band $\pm d$, contactor $\pm a$, and plant function $G(s)$.

Representing 'Bang-Bang' control [12], the dead-band and contactor block introduce non-linearities to the controller. This, coupled with the unknown plant function, makes experimental trial and error the only viable option for determining the gain K_5 . Extensive testing with the desired height set to 25 cm, the dead-band set to ± 5 cm, and the change in throttle set to $\pm 25\%$, yielded an experimental value of 1.5 for K_5 .

6.4 Filters

As mentioned, experimental gain values (especially for angular rates) needed to be reduced due to control surface twitching from motor vibrations at high throttle values. However, extreme reduction of these values alone is not a viable option for reducing control surface response to motor noise. While it would minimize noise, continued reduction would minimize damping in both instances, leading to large overshoots for the ailerons and elevator. Therefore, the gain reduction presented in previous sections must be accompanied by a filter to reduce any remaining noise from the motor. To do so, a simple weighted average type filter was introduced to roll and pitch, and their respective rates. It is modeled as

$$y_o[\text{new}] = (1 - f)y_o[\text{old}] + fy_i[\text{old}] \quad (6.4.1)$$

where f is a filter averaging constant, $y_i[\text{old}]$ is the old sensor input value, $y_o[\text{old}]$ is the old filtered output, and $y_o[\text{new}]$ is the new filtered output. As f tends to zero, more weight is placed on old filtered values, allowing for more smoothing of the signal.

A basic averaging ($f = 0.5$) for roll and pitch proved to be effective in experimental tests to reduce noise at low angular speeds. However, at high throttle values, vibrational noise from the motor heavily affected roll and pitch rate signals, causing unwanted twitching in the control surfaces. As such, heavy smoothing was necessary to counter this, with both rates needing filter constants of 0.2. It should be noted that these filter values did not completely remove motor noise at max throttle, however, they were deemed sufficient for controlled flight. Lastly, motor noise was not prevalent in the distance sensor signals, making filtering the altitude readings unnecessary.

6.5 Summary of Controllers

Below is a table summary of the WIG model controllers that were implemented.

Table 9: Controller summary for the WIG vehicle model.

	Aileron Control	Elevator Control	Throttle Control
Command Signal	$\phi_{cmd} = 0$	$\theta_{cmd} = 2^\circ$	$h_{cmd} = 25 \text{ cm}$
Saturation	$a_A = \pm 25^\circ$	$a_E = \pm 20^\circ$	-
Dead-band	-	-	$d_T = \pm 5 \text{ cm}$
Contactors	-	-	$a_T = \pm 25\%$
Filter Constants	$f_\phi = 0.5, f_p = 0.2$	$f_\theta = 0.5, f_q = 0.2$	-
Theoretical Gains	$K_1 = 1.5, K_2 = 0.05$	$K_3 = -0.4, K_4 = -0.05$	-
Experimental Gains	$K_1 = 0.8, K_2 = 0.02$	$K_3 = -0.3, K_4 = -0.01$	$K_5 = 1.5$

7 Conclusion

The purpose of the WIG demonstrator project is to explore the viability of a WIG vehicle for use on celestial bodies such as Mars and Titan. WIG vehicles utilize the ground effect, which increases lift and reduces drag due to the increased stagnation pressure beneath the wings when flying extremely close to a surface. The ground effect increases the effective aspect ratio of a wing, allowing WIG vehicles to carry a payload with a shorter wingspan than would be possible for a conventional airplane without the ground effect [1]. This reduces both the structural weight and the footprint of the aircraft, which is beneficial for interplanetary missions where size and weight constraints are relevant because the aircraft must fit within a launch vehicle.

The ground effect becomes obsolete when a WIG vehicle flies at an altitude greater than half its wingspan [1]. Since the advantages of WIG vehicles lie in their extremely low-altitude flight, they are only suitable for use over smooth terrain. In near-surface flight, WIG vehicles may skid across the surface and must be constructed to withstand such collisions. WIG vehicles intended for use over liquid bodies must have a hull design that can withstand hydrodynamic loads during takeoff and landing [1]. These considerations, which are less relevant for conventional airplanes, add weight to the design of such vehicles. Additionally, a WIG vehicle is less suitable for use in choppy liquid bodies, where waves rise beyond a half-wingspan above the surface. The vehicle may be damaged by these waves, and foregoes the ground effect if it ascends to avoid them [1]. It is worth noting that a hull design would not be necessary for operation on Mars, but may have significance during operation on Titan due to large bodies of liquid methane on its surface [13] [14].

Another disadvantage of near-surface flight is that roll and pitch mobility are severely reduced, since excessive roll or pitch can cause the wings, nose, or tail to strike the surface. This necessitates automatic aileron and elevator control to keep roll and pitch attitude angles within acceptable bounds. However, any aircraft operating on another celestial body would be equipped with automatic attitude control, regardless of altitude; the control would just need to be extremely precise for a WIG vehicle compared to conventional aircraft.

Overall, the advantages of WIG vehicles make them an attractive alternative to rotorcraft and conventional airplanes for use on celestial bodies with smooth terrain, such as Mars or Titan. Their use of the ground effect reduces the size and weight needed to carry a payload compared to conventional aircraft. A

shorter wingspan also makes the transfer of the vehicle from Earth to the celestial body more feasible, with the main concerns being takeoff and landing once the WIG vehicle has reached its final destination. While the vertical takeoff and landing capabilities of rotorcraft certainly has its advantages, a WIG vehicle will be less prone to inversion during ascent and descent, minimizing the risk of vehicle and mission loss.

8 References

- [1] J. G. Leishman, *Introduction to Aerospace Flight Vehicles*, Embry-Riddle Aeronautical University, 2025, Chap 15.
- [2] Gynn, M. D., Croom, M. A., Smith, S. C., Parks, R. W., and Gelhausen, P. A., *Evolution of a Mars Airplane Concept for the ARES Mars Scout Mission* (AIAA Paper 2003-6578). NASA Technical Reports Server.
- [3] Friedlander B., *Astronomers Estimate Titan's Largest Sea is 1000 Feet Deep*, Cornell Chronicle, 2021.
- [4] *Maritime Safety: Wing-in-Ground (WIG) craft*, International Maritime Organization. Accessed May 11, 2025.
- [5] Anderson, M. R., MAE 155A Winter 2025, *Mass Properties Lecture Notes*. University of California, San Diego, Department of Mechanical and Aerospace Engineering.
- [6] *NACA 4415 Airfoil*, Airfoil Tools. Accessed May 11, 2025.
- [7] Anderson, M. R., MAE 155B Spring 2025, *Preliminary Sizing Lecture Notes*. University of California, San Diego, Department of Mechanical and Aerospace Engineering.
- [8] *Performance Data*, APC Model Aircraft propellers. Accessed April 10, 2025.
- [9] Anderson, M. R., MAE 142 Winter 2025, *Aircraft Modal Analysis Lecture Notes*. University of California, San Diego, Department of Mechanical and Aerospace Engineering.
- [10] Anderson, M. R., MAE 142 Winter 2025, *Describing Functions Lecture Notes*. University of California, San Diego, Department of Mechanical and Aerospace Engineering.
- [11] Franklin, G. F., Powell, J. D., and Emami-Naeini, A., *Feedback Control of Dynamic Systems*, 6th ed., Pearson College Div., 2009, Chap. 3.
- [12] Anderson, M. R., MAE 155B Spring 2025, *Attitude Control Lecture Notes*. University of California, San Diego, Department of Mechanical and Aerospace Engineering.
- [13] *Mars Facts*, National Aeronautics and Space Administration. Accessed May 11, 2025.
- [14] *Cassini Explores a Methane Sea on Titan*, Jet Propulsion Laboratory, April 26, 2016. Accessed May 11, 2025.

9 Appendix

9.1 Stability Derivative Equations

Non-dimensional and dimensional stability derivative equations relevant to roll and short-period mode calculations [12].

$$\begin{aligned}
C_{L\delta E} &= \frac{S_t}{S} \eta \tau C_{L\alpha_t} & C_{m\delta E} &= -\frac{S_t}{S} \frac{x_t}{\bar{c}} \eta \tau C_{L\alpha_t} & C_{l\delta A} &= 2 \frac{S_a y_a}{S b} \tau C_{L\alpha} & \eta &= \left(\frac{V_t}{V}\right)^2 \\
L_{\delta A} &= \frac{\bar{q} S b}{I_{xx}} C_{l\delta A} & L_p &= \frac{\bar{q} S b}{2 I_{xx} V} C_{lp} \\
M_{\delta E} &= \frac{\bar{q} \bar{c} S}{I_{yy}} C_{m\delta E} & M_\alpha &= \frac{\bar{q} \bar{c} S}{I_{yy}} C_{m\alpha} & M_q &= \frac{\bar{q} \bar{c}^2 S}{2 V I_{yy}} C_{mq} \\
Z_{\delta E} &= \frac{-\bar{q} S}{m} C_{L\delta E} & Z_\alpha &= \frac{-\bar{q} S}{m} (C_{D0} + C_{L\alpha}) & Z_q &= \frac{-\bar{q} \bar{c} S}{2 m V} C_{Lq}
\end{aligned}$$